

#### Contents lists available at ScienceDirect

## Ultramicroscopy

journal homepage: www.elsevier.com/locate/ultramic



# Direct determination of structural heterogeneity in metallic glasses using four-dimensional scanning transmission electron microscopy



Soohyun Im<sup>a</sup>, Zhen Chen<sup>b</sup>, Jared M. Johnson<sup>a</sup>, Pengyang Zhao<sup>a</sup>, Geun Hee Yoo<sup>c</sup>, Eun Soo Park<sup>c</sup>, Yunzhi Wang<sup>a</sup>, David A. Muller<sup>b,d</sup>, Jinwoo Hwang<sup>a,\*</sup>

- <sup>a</sup> Department of Materials Science and Engineering, The Ohio State University, Columbus, OH 43212, USA
- <sup>b</sup> School of Applied and Engineering Physics, Cornell University, Ithaca, NY 14853, USA
- C Department of Materials Science and Engineering, Research Institute of Advanced Materials, Seoul National University, Seoul 08826, South Korea
- <sup>d</sup> Kavli Institute at Cornell for Nanoscale Science, Cornell University, Ithaca, NY 14853, USA

#### ABSTRACT

We report the first direct quantification of the structural heterogeneity in metallic glasses using intensity variance and angular correlation analyses of the 4-dimensional (4-D) scanning transmission electron microscopy (STEM) data. We demonstrate that the real-space reconstruction and analyses of the 4-D nanodiffraction data acquired using a pixelated fast STEM detector enables quantitative determination of the details of local structural heterogeneity, including the type, size, volume fraction and spatial distribution of local ordering at the nano- to meso-scale, beyond the limits of the previous measurements using conventional detectors. We show that different types of local ordering are present in  $Zr_{55}Co_{25}Al_{20}$  glass, leading to a high degree of structural heterogeneity, with the total volume of locally ordered regions making up to  $\sim 14\%$  of the entire volume. These findings are significant, as the structure-property relationship in metallic glasses and other amorphous materials has been difficult to establish because of the lack of detailed structural information from experiments.

Understanding the properties of amorphous materials is often complicated by the difficulties in determining the structural origin of the observed properties. This is largely due to the challenges in characterizing their structures, as the inherent disordered arrangement of atoms makes the characterization much more complex than that of the ordered arrangement of atoms in crystalline materials. The prime example of this ongoing challenge is in the study of metallic glasses (MGs), where understanding the detailed mechanism of their plastic deformation has remained as one of the most critical issues [1-3]. Over the last decade, significant progress has been made in gaining such understanding using both experimental [4-7] and theoretical [8-12] approaches. However, one of the important remaining challenges is to determine how the structure is correlated to the deformation of MGs. The current theory of MG deformation involves the activation of shear transformation zones (STZs) upon thermal-mechanical loading [13]. While the STZs are usually manifested in dynamic local inelastic events, the question is whether or how such events are affected by the local atomic structures of the MGs. Such an explicit correlation between the structure and deformation, if established, would be able to explain, for example, why some MGs are much more ductile than others [14,15], and why such differences in ductility can be induced by only a small change in their composition or thermal history [16,17]. The correlation would also provide new opportunities to tune the structure to simultaneously achieve multiple desired properties, for example, both high strength and ductility, which is one of the ultimate goals in the development of new generation structural materials.

In this study, we focus on understanding the details of the structural heterogeneity in MGs. Structural heterogeneity has been recently observed both in experiments [18-21] and simulations [22,23], which have suggested that the length scale of the heterogeneity may be at about one to a few nanometers. The heterogeneity may be inherent to the structure of the glass-forming liquid prior to quenching [22], but the measured heterogeneity in an MG at room temperature is unarguably static in nature. Even so, the heterogeneity may still be inherently coupled to the local deformation event [24], especially at the length scale of an STZ which is also proposed to be about one to a few nanometers. This emphasizes the importance of accurate experimental characterization of the heterogeneity in establishing fundamental understanding of the structure-deformation relationships in MGs. While electron nanodiffraction studies have previously revealed a few types of medium range ordering (MRO) [18,25] that may constitute the heterogeneity, there are still other important structural parameters of MRO, for example, their average size (length scale), volume fraction, and spatial distribution (or correlation), that have been shown critically important in determining the deformation behavior of an MG (e.g. [24,26]), but remained difficult to be directly characterized so far.

E-mail address: hwang.458@osu.edu (J. Hwang).

<sup>\*</sup> Corresponding author.

S. Im et al. Ultramicroscopy 195 (2018) 189-193

Determining accurately such parameters requires new characterization capabilities beyond the limits of the methods used previously.

Here we report the first direct determination of the type, size, volume fraction, and spatial distribution of nanoscale heterogeneity in an MG using 4-dimensional (4-D) scanning transmission electron microscopy (STEM) [27]. 4-D STEM uses the new-generation pixelated fast STEM detectors with high sensitivity that enable the acquisition of individual 2-D diffraction patterns from every single probe position within the 2-D sample area. Using the angular correlation function [28] and intensity variance [29] analyses of the 4-D data, we show that the MG structure contains multiple randomly distributed types of MRO regions with different rotational symmetries and an average size of  $\sim 1.3$  nm, making up  $\sim 14\%$  of the material's volume. The implication of this new characterization is significant, as the heterogeneity we determined here could provide not only new insights into possible correlations between structure and deformation behavior of MGs, but also direct inputs to deformation simulations at both the atomistic [11,24] and meso [26,30-32] scales to establish robust structure-property relationships.

For this study, we prepared  $Zr_{55}Co_{25}Al_{20}$  alloy ingots using arcmelting with high purity elements of Zr (99.9%), Co (99.9%) and Al (99.9%) under Ti-gettered argon atmosphere. The ingot was re-melted more than six times to ensure compositional homogeneity and the remelting process was completed within a minute.  $Zr_{55}Co_{25}Al_{20}$  metallic glass ribbons were synthesized by a melt spinning technique. The alloy ingot was re-melted in a quartz tube in an induction heater, and was ejected with an over-pressure of 50 kPa through a 1.2 mm-diameter circular nozzle onto a copper wheel rotating with a surface velocity of 20 m/s. The dimension of the as-spun ribbons was 4.5  $\pm$  0.2 mm in width and 75  $\pm$  5  $\mu$ m in thickness. TEM specimens were prepared using the standard lift-out method in a focused ion beam, using ion beam energies of 30 kV and 5 kV. Low energy ion mill was used at 500 V to further thin and clean the surface of the sample.

4-D STEM was performed using a Thermo Fisher Scientific Titan Themis STEM equipped with a fast high dynamical range EMPAD pixelated STEM detector [27], operated at 300 kV. A one nanometer-sized probe was formed using a  $50\,\mu\mathrm{m}$  C<sub>2</sub> aperture and convergence half angle of  $1.15\,\mathrm{mrad}$ . Each diffraction pattern has 128 by 128 pixels (a pixel size is  $0.16\,\mathrm{nm}^{-1}$ ) and was collected using a 1 ms exposure time. The detector readout time is  $0.86\,\mathrm{ms}$ . The nanodiffraction stacks were analyzed using both the Cornell Spectrum Imager [33] and Igor Pro software. At the magnification of  $2.55\,\mathrm{Mx}$ , scanning step size of  $0.32\,\mathrm{nm}$ , and 128 by 128 scanning points, one 4-D nanodiffraction dataset covers approximately a 40 by  $40\,\mathrm{nm}^2$  area of the sample, with

oversampling of the probe positions (Fig. 1a). The oversampling, which is now technically feasible due to the fast acquisition rate of the detector [27,34,35], is important as it captures the gradual change in the measured structure along the scan direction. From the acquired diffraction stack (Fig. 1b), we can choose any pixel  $(k_x, k_y)$  or any area in the diffraction plane to reconstruct the real space image that has the corresponding pixel (or integrated) intensities for the same probe (i.e. pixel) positions (Fig. 1c). For example, selecting a pixel at the center of the diffraction pattern (where the zero beam is) will result in a bright field image (not shown), and selecting a pixel near the diffraction speckles (e.g. points e or f in Fig. 1d) will result in a dark field (DF) image (Fig. 1e and f. respectively). It is worth noticing that the two DF images (Fig. 1e and f) differ significantly from each other, even though they are formed at the same scattering vector magnitude, k. This is because each image only captures the MRO regions that are diffracting to that particular direction.

The possible identification of MRO using DF images has been the subject of previous studies (e.g. [36]). In the earlier studies, the DF images were acquired by tilting the illumination to  $(-k_x, -k_y)$  position and placing a small objective aperture at the optical axis (a.k.a. tilted-DF), or using the hollow-cone illumination to integrate all the diffraction signals for the same k (which would be similar to using an unusually thin annular DF (ADF) detector in STEM). However, these approaches may involve some complications. In the tilted-DF mode, for example, the image may significantly undersample the MRO regions because it only captures the MRO diffraction at a particular *k* direction. Hollow-cone illumination, on the other hand, can capture the MRO signals at all k directions, and also reduce noisy speckles that may arise from random correlations [29,37]. However, the contrast of MRO speckles is substantially suppressed in the hollow-cone images, which tends to make the direct identification of some of the important MRO parameters, such as the size and volume fraction, rather challenging. The DF images may also contain intensities due to some factors not intrinsic to the structure, such as sample thickness variation [20].

To avoid these issues, we have calculated the 2-D intensity variance,  $V_{2D}(\varphi)$ , among the DF images,  $I_{2D}(\varphi)$ , that are formed using the pixels with same k, annularly distributed over the angle  $\varphi$ . The rationale for this method is that any structural variance due to the heterogeneity will be more emphasized in  $V_{2D}(\varphi)$ , as compared to hollow-cone TEM or ADF STEM where the annular integration of the intensity,  $\langle I_{2D}(\varphi) \rangle_{\varphi}$ , will substantially subdue the intensity variation. In other words,  $V_{2D}(\varphi)$  provides the ability to differentiate the local MRO regions that are all in diffracting (i.e., Bragg) conditions but randomized in their in-plane rotation angle  $\varphi$ . The  $V_{2D}(\varphi)$  method conceptually aligns with the

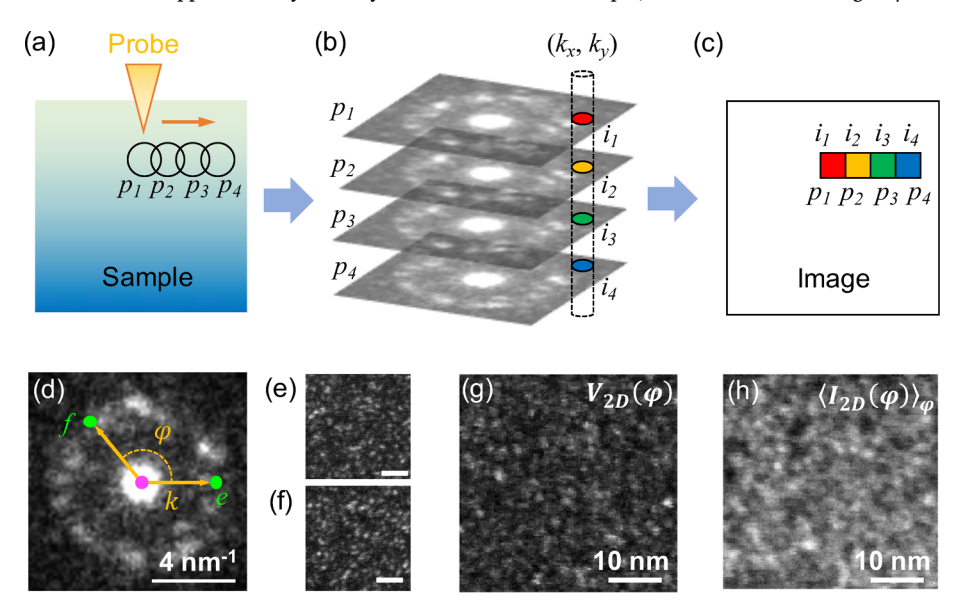
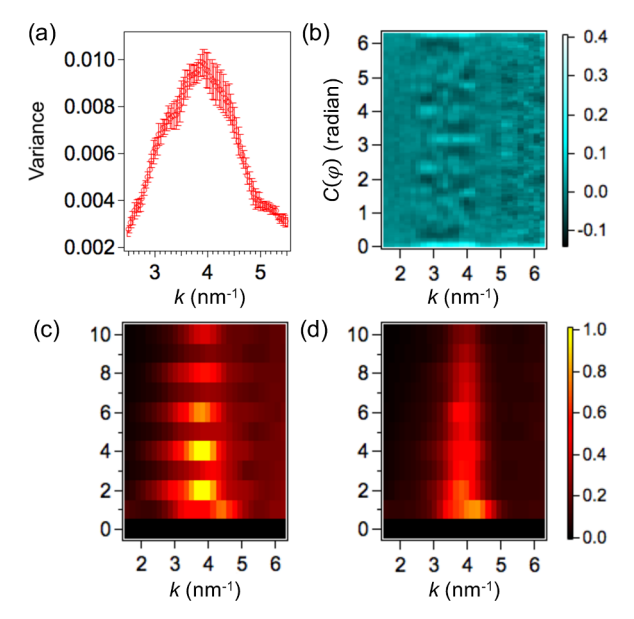


Fig. 1. (color online). (a) to (c) Schematic of 4-D scanning nanodiffraction. (a) The (size = 1 nm) is scanned with oversampling and the dwell time of 1 ms. (b) The diffraction patterns generated from each probe position,  $p_1$  to  $p_4$ , are recorded on the pixelated detector. (c) Any pixel  $(k_x, k_y)$ or area in the diffraction space can be chosen to reconstruct the real space image that will have the corresponding intensity,  $i_1$  to  $i_4$ , for the same probe positions,  $p_1$  to  $p_4$ . (d) shows a pattern among the stack in (b), and the DF images in (e) and (f) are formed using the pixel positions e and f indicated in (d), respectively. The scale bars in (e) and (f) are both 10 nm. Images showing the (g) 2-D variance,  $V_{2D}(\varphi)$ , and (h) averaged intensity,  $\langle I_{2D}(\varphi) \rangle_{\varphi}$ , over  $\varphi$  at  $k = 4 \, \text{nm}^{-1}$ .

S. Im et al. Ultramicroscopy 195 (2018) 189-193



**Fig. 2.** (color online). (a) V(k) measured from the  $\mathrm{Zr}_{55}\mathrm{Co}_{25}\mathrm{Al}_5$  MG using the nanodiffraction patterns acquired using Gatan Ultrascan CCD camera. It shows the peak at  $k=4\,\mathrm{nm}^{-1}$ , suggesting that the degree of structural fluctuation (heterogeneity) is the highest at that k value. (b) An angular correlation function over  $\varphi$  as a function of k, calculated from one of the diffraction patterns. (c) The averaged power spectrum of the angular correlation function over the entire sample area of a thin sample (~20 nm thick). (d) The averaged power spectrum from a thick area of the sample (~42 nm thick).

calculation of variance as a function of k, or V(k), commonly known as fluctuation microscopy [29], but the difference is that  $V_{2D}(\varphi)$  preserves all the spatial information in 2-D, while V(k) typically loses the 2-D information. The calculation of  $V_{2D}(\varphi)$  is enabled in the 4-D STEM because it can resolve all the DF images as a function of  $\varphi$ , or  $I_{2D}(\varphi)$ . In a conventional TEM or STEM, this would require acquiring many DF images by continuously displacing the objective aperture over the angle  $\varphi$ , which is technically challenging and highly inefficient. We calculated  $V_{2D}(\varphi)$  using  $V_{2D}(\varphi) = [\langle I_{2D}(\varphi)^2 \rangle_{\varphi} - \langle I_{2D}(\varphi) \rangle_{\varphi}^2]/\langle I_{2D}(\varphi) \rangle_{\varphi}^2$ , at  $k = 4 \text{ nm}^{-1}$  where V(k) shows the highest peak (Fig. 2a). The interval between the angle  $\varphi$ , or  $\Delta \varphi$ , was set to be 10°, according to the Bragg acceptance angle (the average maximum angle that one diffraction speckle spans over the  $\varphi$  range) defined previously [38]. As a result,  $V_{2D}(\varphi)$  formed at  $k = 4 \,\mathrm{nm}^{-1}$  (Fig. 1g) is quite different from <  $I_{2D}(\varphi) > \omega$  at the same k from the same area (Fig. 1h). As explained above, the speckles in  $V_{2D}(\varphi)$  should represent the MRO regions more accurately as compared to those in  $\langle I_{2D}(\varphi) \rangle_{\omega}$ , and this will be confirmed when combined with the angular correlation analysis described

We further analyzed the type of MRO by calculating the angular correlation function of the intensity in each nanodiffraction pattern. When the probed volume contains an ordered region, the diffraction intensity from that region will be much stronger and more directional as compared to the diffused scattering from the disordered regions and, therefore, the angular correlation function tends to reveal the structural symmetry of the local MRO within the probed volume [39,40]. Since we scan the material using 1 nm-sized probes, the diffraction patterns will be dominated by the diffraction from nanoscale MRO regions, rather than from the smaller nearest-neighbor clusters (~0.5 nm in length) that have been often identified as the structural unit in atomistic simulations (see e.g. [41]). For a given k, the angular correlation,  $C(\varphi)$ , is  $C(\varphi) = [\langle I(\theta)I(\theta + \varphi)\rangle_{\theta} - \langle I(\theta)\rangle_{\theta}^{2}]/\langle I(\theta)\rangle_{\theta}^{2}$ , where  $\theta$ ranges from 0 to  $2\pi$  radian [28]. Fig. 2b shows an example of  $C(\varphi)$ calculated from one of the nanodiffraction patterns as a function of k. The Fourier transform of each  $C_k(\varphi)$  can be calculated to reveal the constituent sinusoidal functions that have the frequency of n. n depends

on how many peaks the  $C_k(\varphi)$  has within one period  $(0 - 2\pi)$  and, therefore, it can represent the rotational symmetry present within the pattern. Fig. 2c shows the power spectrum calculated from each  $C(\varphi)$ averaged over the entire diffraction stack acquired from the sample region shown in Fig. 1. It shows high amplitude for the even numbered frequencies (n = 2, 4, 6, ...), suggesting that some nanoscale regions strongly diffract the electrons and show patterns that have even numbered symmetries (i.e. 2-, 4-, and 6-fold, ..). The power spectrum would show no peak if the structure is completely disordered (or homogeneous) at the length scale of the probe size (1 nm), and therefore Fig. 2c suggests that high degree of heterogeneity is present within the MG structure at the length scale of  $\sim 1$  nm. It is also worth noting that the rotational symmetry appeared in the data should be influenced by Friedel symmetry. For example, the 5-fold symmetry in the structure, if exist, should appear as 10-fold when the TEM sample thickness is sufficiently thin.

While Fig. 2c indicates the heterogeneity involving nanoscale MRO, the question of whether we can interpret each n value as indicative of a particular MRO structure still remains. In general, any attempt to define a deterministic structural motif in MGs can be misleading because, after all, the structure is still amorphous. In past studies involving atomistic modeling, MRO with a certain symmetry, for example, 5-fold (or 10fold with its conjugate) or 6-fold, has been identified as icosahedral MRO or "crystalline-like" MRO (e.g. [18,22]), respectively. However, since the present work relies only on the experimental data without any input from atomistic modeling or simulation, we would like to reserve such distinction and present the data as is to avoid any potential misunderstanding, although it is certainly possible that each n value may represent a different type of MRO. Some potential errors intrinsic to the angular correlation analysis have been previously identified [42], but in addition to those, here we also found that the amplitude of the odd numbered n's increases as the thickness of the TEM foil increases (Fig. 2d). This may indicate that the odd numbered n's may include some artifacts due to plural scattering. The odd numbered symmetries could also be related to the breakdown of Friedel symmetry with increasing sample thickness reported in the previous work [40]. Hence, for the following analysis, we only used data from very thin areas of the sample (~20 nm thick, such as the one shown in Fig. 2c), and avoided using the odd numbered n's in the analysis.

Based on the power spectrum calculated for each probe position, we constructed the spatial map for each n-fold symmetry for even numbered *n*'s, which is shown in Fig. 3a to e (the maps for n = 1 and 3 are also provided in Fig. S1 for comparison). The maps are also overlaid with a contour map (gray lines) of the  $V_{2D}(\varphi)$  shown in Fig. 1g for comparison. The hotspots in each map indicate the pixels whose corresponding n value is high, meaning that they indicate the regions where the n-fold signal is strong. Therefore, these hotspots can be considered as the MRO regions showing a strong local symmetry. Based on the size of the hotspots, the MRO regions appear to be about one to a few nanometers in diameter, which is consistent with the previous fluctuation microscopy results [18,20]. More quantitative analysis of the MRO size is provided in the next section. In all of the maps from Fig. 3a to e, the hotspots are mostly confined within the contour lines of the bright speckles in the overlaid  $V_{2D}(\varphi)$ , confirming that most of the bright features in  $V_{2D}(\varphi)$  (Fig. 1g) are indeed the diffraction speckles from MRO regions that have strong structural symmetry. As indicated by the intensity scale bars for each map, the n = 2 and 4 maps show the strongest signal, and n = 8 and 10 signals appear to be relatively weak, and this is consistent with the trend in the averaged power spectrum data shown in Fig. 2c. However, this should not necessarily be interpreted as the degree of ordering being higher when n is lower, because the diffracted intensities can be distributed among the speckles and therefore the intensity per speckle will become lower as n increases. Fig. 3f shows the normalized sum of all the maps shown in Fig. 3a to e, and it also qualitatively confirms that most of the hotspots are confined within the speckle positions in  $V_{2D}(\varphi)$ . Very similar results were also

S. Im et al. Ultramicroscopy 195 (2018) 189-193

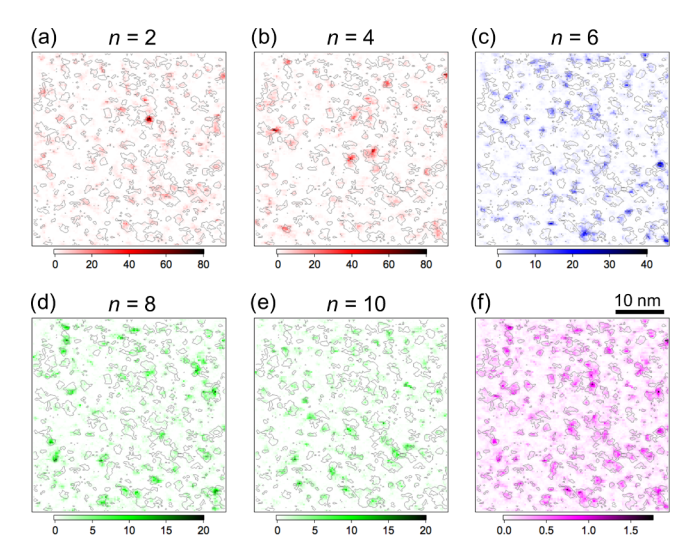


**Fig. 3.** (color online). (a to e) Power spectrum amplitude of each nanodiffraction pattern spatially mapped over the entire sample area for each n value. Different color scale represents the different maximum intensity in each map. For comparison, the maps are overlaid with the contour map (gray lines) that represents the bright speckles in the  $V_{2D}(\varphi)$  map shown in Fig. 1g. (f) shows the normalized sum of all the maps from (a) to (e), which shows the overall qualitative match between the power spectrum intensity and  $V_{2D}(\varphi)$ .

obtained from other thin areas of the sample (see Fig. S2).

We calculated the size and volume fraction of the hotspot (MRO) regions for each n by applying the standard particle analysis routine (Fig. 4a) onto each map shown in Fig. 3. Here we used two simple assumptions, one is that each MRO has spherical shape on average, and the other is that the Bragg acceptance angle is  $10^{\circ}$  [38], which provides the percentage of the MRO regions that are in the diffracting conditions to the ones that are not (5.9%). The latter is important because Fig. 3 shows only the MRO regions that are in the diffracting conditions. The total volume of the material shown in Fig. 3 is  $\sim 32,970 \, \text{nm}^3$ , calculated based on the area (40.6 by  $40.6 \, \text{nm}^2$ ) and the thickness of the sample ( $\sim 20 \, \text{nm}$ ) estimated from the electron transmittance [20]. The result shows that the average diameter of the MRO regions is  $1.3 \pm 0.08 \, \text{nm}$ , indicating fairly uniform MRO sizes throughout the n values, although n=4 and n=8 showed slightly larger diameter than the others

(Fig. 4b). Volume fraction of MRO showed more variation, 2.8  $\pm$  0.3%, with n=4 being noticeably lower than others ( $\sim$ 2.2%), which may indicate that n=4 MROs tend to be bigger but fewer in quantity than others. The sum of all volume fraction among n's from 2 to 10 is  $\sim$ 13.8%, and this is higher than the volume fraction calculated from the integrated map shown in Fig. 3f ( $\sim$ 7.5%), which indicates that some MRO regions overlap between the maps.

We also calculated the 2-D autocorrelation function,  $\sigma$ , as a function of distance, r, for each map shown in Fig. 3.  $\sigma(r)$  for low r, shown in Fig. 4c, may provide another way to make the size comparison between the MROs with different n's. However, the direct comparison of their sizes is still challenging because  $\sigma(r)$  is still dependent on the power spectrum amplitude, which decreases as n increases (Fig. 2c). Still, it does provide some interesting information, for example, n = 4 extends over longer r compared to n = 2, even though n = 2 has slightly higher power spectrum amplitude. This indicates that the MRO regions with n = 4 may have larger sizes than others on average, which is also consistent with the data shown in Fig. 4b. At the longer length scale,  $\sigma(r)$  clearly shows a 'nearest-neighbor' peak appearing within 4 < r < 6 range for n = 2, 4, and 6 (Fig. 4d), indicating that there may be some spatial correlation among the MRO regions. However, it is important to remind that this is only the correlation among the MRO regions that are in diffracting conditions, and therefore the data does not capture the full correlation among the same MRO types in 3-dimension.

By advancing fluctuation microscopy and angular correlation analyses of 4-D STEM data, new important information on MRO and structural heterogeneity in  $\rm Zr_{55}Co_{25}Al_{20}$  MG has been identified. Our work presents a new way to precisely determine the details of the MRO, including size, volume fraction, and spatial distribution of each MRO type in a large volume of the sample. The implication of this result is significant, as variations in structural heterogeneity caused by, for example, a small change in composition or thermal history, could be responsible for changes in properties that were previously observed. It is also important to emphasize that the types of MRO measured in this work are not always present in molecular dynamics simulations of MG structures (with only a few exceptions (e.g. [22])). Therefore, the experimentally determined heterogeneity can also inform and guide deformation simulations at both the atomistic and mesoscale levels to establish more robust structure-property relationship in MGs.

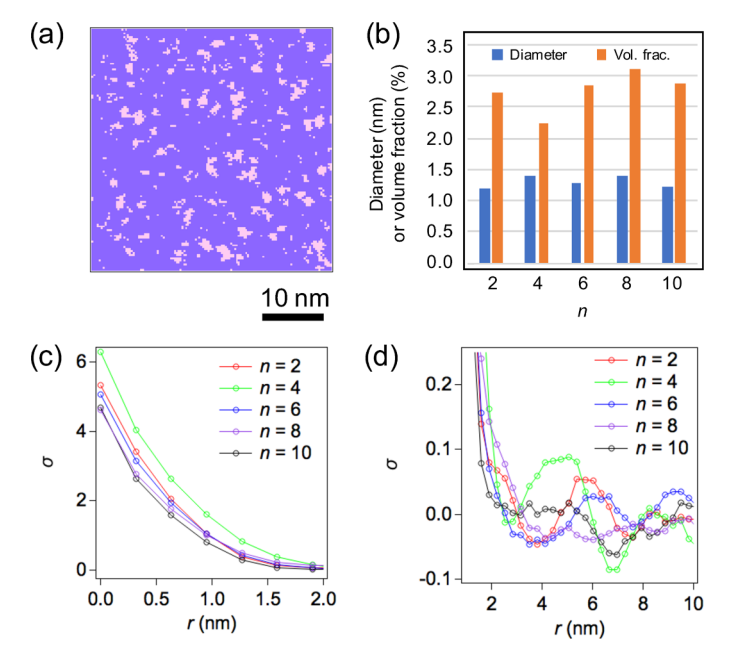


**Fig. 4.** (color online). (a) A map same as the one shown in Fig. 3f but applied with a threshold value to perform the MRO size and volume fraction analyses. The threshold value was determined using the iterative method in Igor Pro software. From the map, the number (87 total) and the average size of the MRO regions (radius  $\sim 0.74\,\mathrm{nm}$ ) were determined. (b) Bar graphs showing the diameter and volume fraction of MRO for each n value. (c) Autocorrelation function,  $\sigma$ , among the pixel intensity as a function of distance, r, calculated for each power spectrum map shown in Fig. 3. (d) Same correlation function,  $\sigma(r)$ , shown in (c), but at a longer length (r) scale.

#### Acknowledgment

S. I, P. Z, Y. W, and J. H. acknowledge support by the NSF under DMR-1709290. This work was performed in part at the Cornell PARADIM Electron Microcopy Facility, as part of the Materials for Innovation Platform Program, which is supported by the NSF under DMR-1539918 with additional infrastructure support from DMR-1719875 and DMR-1429155.

### Supplementary materials

Supplementary material associated with this article can be found, in the online version, at doi:10.1016/j.ultramic.2018.09.005.

#### References

- [1] A.L. Greer, Y.Q. Cheng, E. Ma, Shear bands in metallic glasses, Mater. Sci. Eng. R Reports. 74 (2013) 71–132 http://dx.doi.org/10.1016/j.mser.2013.04.001.
- [2] C.A. Schuh, T.C. Hufnagel, U. Ramamurty, Mechanical behavior of amorphous alloys, Acta Mater 55 (2007) 4067–4109 https://doi.org/10.1016/j.actamat.2007.01.052
- [3] T.C. Hufnagel, C.A. Schuh, M.L. Falk, Deformation of metallic glasses: Recent developments in theory, simulations, and experiments, Acta Mater 109 (2016) 375–393 https://doi.org/10.1016/j.actamat.2016.01.049.
- [4] W.H. Jiang, M. Atzmon, Room-temperature flow in a metallic glass Strain-rate dependence of shear-band behavior, J. Alloys Compd 509 (2011) 7395–7399 https://doi.org/10.1016/j.jallcom.2011.04.041.
- [5] C.A. Schuh, T.G. Nieh, A nanoindentation study of serrated flow in bulk metallic glasses, Acta Mater 51 (2003) 87–99 https://doi.org/10.1016/S1359-6454(02) 00303-8.
- [6] T. Burgess, M. Ferry, Nanoindentation of metallic glasses, Mater. Today. 12 (2009) 24–32 https://doi.org/10.1016/S1369-7021(09)70039-2.
- [7] J. Kim, H.S. Oh, W. Kim, P.-P. Choi, D. Raabe, E.S. Park, Modulation of plastic flow in metallic glasses via nanoscale networks of chemical heterogeneities, Acta Mater 140 (2017) 116–129 https://doi.org/10.1016/j.actamat.2017.08.002.
- [8] M.L. Falk, J.S. Langer, L. Pechenik, Thermal effects in the shear-transformation-zone theory of amorphous plasticity: Comparisons to metallic glass data, Phys. Rev. E. 70 (2004) 11507 https://link.aps.org/doi/10.1103/PhysRevE.70.011507.
- [9] Y. Shi, M.L. Falk, Atomic-scale simulations of strain localization in three-dimensional model amorphous solids, Phys. Rev. B. 73 (2006) 214201https://link.aps.org/doi/10.1103/PhysRevB.73.214201.
- [10] E.R. Homer, C.A. Schuh, Mesoscale modeling of amorphous metals by shear transformation zone dynamics, Acta Mater. 57 (2009) 2823–2833 https://doi.org/ 10.1016/j.actamat.2009.02.035.
- [11] Y. Fan, T. Iwashita, T. Egami, Crossover from Localized to Cascade Relaxations in Metallic Glasses, Phys. Rev. Lett. 115 (2015) 45501 https://link.aps.org/doi/10. 1103/PhysRevLett.115.045501.
- [12] Y. Fan, T. Iwashita, T. Egami, How thermally activated deformation starts in metallic glass, Nat. Commun. 5 (2014) 5083 http://dx.doi.org/10.1038/ncomms6083.
- [13] A.S. Argon, Plastic deformation in metallic glasses, Acta Metall 27 (1979) 47–58 https://doi.org/10.1016/0001-6160(79)90055-5.
- [14] J. Schroers, W.L. Johnson, Ductile Bulk Metallic Glass, Phys. Rev. Lett. 93 (2004) 255506https://link.aps.org/doi/10.1103/PhysRevLett.93.255506.
- [15] B. Zhang, D.Q. Zhao, M.X. Pan, W.H. Wang, A.L. Greer, Amorphous Metallic Plastic, Phys. Rev. Lett. 94 (2005) 205502https://link.aps.org/doi/10.1103/PhysRevLett. 94 205502.
- [16] J.M. Park, J.H. Han, N. Mattern, D.H. Kim, J. Eckert, Designing Zr-Cu-Co-Al Bulk Metallic Glasses with Phase Separation Mediated Plasticity, Metall. Mater. Trans. A. 43 (2012) 2598–2603, https://doi.org/10.1007/s11661-011-1050-z.
- [17] E.S. Park, H.J. Chang, J.S. Kyeong, D.H. Kim, Role of minor addition of metallic alloying elements in formation and properties of Cu-Ti-rich bulk metallic glasses, J. Mater. Res 23 (2008) 1995–2002, https://doi.org/10.1557/JMR.2008.0246.
- [18] J. Hwang, Z.H. Melgarejo, Y.E. Kalay, I. Kalay, M.J. Kramer, D.S. Stone, P.M. Voyles, Nanoscale Structure and Structural Relaxation in Zr50Cu45Al5 Bulk Metallic Glass, Phys. Rev. Lett. 108 (2012) 195505https://link.aps.org/doi/10. 1103/PhysRevLett.108.195505.
- [19] Y.E. Kalay, J. Kalay, J. Hwang, P.M. Voyles, M.J. Kramer, Local chemical and to-pological order in Al–Tb and its role in controlling nanocrystal formation, Acta Mater 60 (2012) 994–1003 https://doi.org/10.1016/j.actamat.2011.11.008.
- [20] J. Hwang, P.M. Voyles, Variable Resolution Fluctuation Electron Microscopy on Cu-Zr Metallic Glass Using a Wide Range of Coherent STEM Probe Size, Microsc. Microanal. 17 (2011) 67–74, https://doi.org/10.1017/S1431927610094109.

- [21] J. Hwang, A.M. Clausen, H. Cao, P.M. Voyles, Reverse Monte Carlo structural model for a zirconium-based metallic glass incorporating fluctuation microscopy mediumrange order data, J. Mater. Res. 24 (2009) 3121–3129, https://doi.org/10.1557/ jmr.2009.0386.
- [22] H. Tanaka, T. Kawasaki, H. Shintani, K. Watanabe, Critical-like behaviour of glass-forming liquids, Nat. Mater. 9 (2010) 324 http://dx.doi.org/10.1038/nmat2634.
- [23] M. Leocmach, J. Russo, H. Tanaka, Importance of many-body correlations in glass transition: An example from polydisperse hard spheres, J. Chem. Phys. 138 (2013) 12A536, https://doi.org/10.1063/1.4769981.
- [24] J. Ding, S. Patinet, M.L. Falk, Y. Cheng, E. Ma, Soft spots and their structural signature in a metallic glass, Proc. Natl. Acad. Sci. 111 (2014) 14052–14056 http://www.pnas.org/content/111/39/14052.abstract.
- [25] A. Hirata, P. Guan, T. Fujita, Y. Hirotsu, A. Inoue, A.R. Yavari, T. Sakurai, M. Chen, Direct observation of local atomic order in a metallic glass, Nat. Mater. 10 (2010) 28 http://dx.doi.org/10.1038/nmat2897.
- [26] P. Zhao, J. Li, J. Hwang, Y. Wang, Influence of nanoscale structural heterogeneity on shear banding in metallic glasses, Acta Mater 134 (2017) 104–115 https://doi. org/10.1016/j.actamat.2017.05.057.
- [27] M.W. Tate, P. Purohit, D. Chamberlain, K.X. Nguyen, R. Hovden, C.S. Chang, P. Deb, E. Turgut, J.T. Heron, D.G. Schlom, D.C. Ralph, G.D. Fuchs, K.S. Shanks, H.T. Philipp, D.A. Muller, S.M. Gruner, High Dynamic Range Pixel Array Detector for Scanning Transmission Electron Microscopy, Microsc. Microanal. 22 (2016) 237–249, https://doi.org/10.1017/S1431927615015664.
- [28] P. Wochner, C. Gutt, T. Autenrieth, T. Demmer, V. Bugaev, A.D. Ortiz, A. Duri, F. Zontone, G. Grübel, H. Dosch, X-ray cross correlation analysis uncovers hidden local symmetries in disordered matter, Proc. Natl. Acad. Sci. 106 (2009) 11511–11514, https://doi.org/10.1073/pnas.0905337106.
- [29] M.M.J. Treacy, J.M. Gibson, L. Fan, D.J. Paterson, I. McNulty, Fluctuation microscopy: a probe of medium range order, Reports Prog. Phys. 68 (2005) 2899 http://stacks.iop.org/0034-4885/68/i=12/a=R06.
- [30] Y. Wang, M. Li, J. Xu, Toughen and harden metallic glass through designing statistical heterogeneity, Scr. Mater. 113 (2016) 10–13 https://doi.org/10.1016/j.scriptamat.2015.09.038.
- [31] P. Zhao, J. Li, Y. Wang, Heterogeneously randomized STZ model of metallic glasses: Softening and extreme value statistics during deformation, Int. J. Plast. 40 (2013) 1–22 https://doi.org/10.1016/j.ijplas.2012.06.007.
- [32] P. Zhao, J. Li, Y. Wang, Extended defects, ideal strength and actual strengths of finite-sized metallic glasses, Acta Mater. 73 (2014) 149–166 https://doi.org/10. 1016/j.actamat.2014.03.068.
- [33] R. Hovden, P. Cueva, J.A. Mundy, D.A. Muller, The Open-Source Cornell Spectrum Imager, Micros. Today. 21 (2013) 40–44, https://doi.org/10.1017/ S1551929512000995.
- [34] J.A. Mir, R. Clough, R. MacInnes, C. Gough, R. Plackett, I. Shipsey, H. Sawada, I. MacLaren, R. Ballabriga, D. Maneuski, V. O'Shea, D. McGrouther, A.I. Kirkland, Characterisation of the Medipix3 detector for 60 and 80keV electrons, Ultramicroscopy 182 (2017) 44–53 https://doi.org/10.1016/j.ultramic.2017.06.
- [35] H. Yang, I. MacLaren, L. Jones, G.T. Martinez, M. Simson, M. Huth, H. Ryll, H. Soltau, R. Sagawa, Y. Kondo, C. Ophus, P. Ercius, L. Jin, A. Kovács, P.D. Nellist, Electron ptychographic phase imaging of light elements in crystalline materials using Wigner distribution deconvolution, Ultramicroscopy 180 (2017) 173–179 https://doi.org/10.1016/j.ultramic.2017.02.006.
- [36] J.M. Gibson, M.M.J. Treacy, Diminished Medium-Range Order Observed in Annealed Amorphous Germanium, Phys. Rev. Lett. 78 (1997) 1074–1077 https:// link.aps.org/doi/10.1103/PhysRevLett.78.1074.
- [37] A. Rezikyan, Z.J. Jibben, B.A. Rock, G. Zhao, F.A.M. Koeck, R.F. Nemanich, M.M.J. Treacy, Speckle Suppression by Decoherence in Fluctuation Electron Microscopy, Microsc. Microanal. 21 (2015) 1455–1474, https://doi.org/10.1017/ S1431927615015135.
- [38] W.G. Stratton, P.M. Voyles, A phenomenological model of fluctuation electron microscopy for a nanocrystal/amorphous composite, Ultramicroscopy 108 (2008) 727–736 https://doi.org/10.1016/j.ultramic.2007.11.004.
- [39] J.M. Gibson, M.M.J. Treacy, T. Sun, N.J. Zaluzec, Substantial Crystalline Topology in Amorphous Silicon, Phys. Rev. Lett. 105 (2010) 125504https://link.aps.org/doi/ 10.1103/PhysRevLett.105.125504.
- [40] A.C.Y. Liu, M.J. Neish, G. Stokol, G.A. Buckley, L.A. Smillie, M.D. de Jonge, R.T. Ott, M.J. Kramer, L. Bourgeois, Systematic Mapping of Icosahedral Short-Range Order in a Melt-Spun Zr<sub>36</sub>Cu<sub>64</sub> Metallic Glass, Phys. Rev. Lett. 110 (2013) 205505https://link.aps.org/doi/10.1103/PhysRevLett.110.205505.
- [41] H.W. Sheng, W.K. Luo, F.M. Alamgir, J.M. Bai, E. Ma, Atomic packing and short-to-medium-range order in metallic glasses, Nature 439 (2006) 419 http://dx.doi.org/10.1038/nature04421.
- [42] T. Sun, M.M.J. Treacy, T. Li, N.J. Zaluzec, J. Murray Gibson, The Importance of Averaging to Interpret Electron Correlographs of Disordered Materials, Microsc. Microanal. 20 (2014) 627–634, https://doi.org/10.1017/S1431927613014116.